

A theoretical investigation of a magnetically shielded Hall thruster with conducting walls

J. Perales-Díaz,^{1, a)} A. Domínguez-Vázquez,² and E. Ahedo¹

¹⁾ *Universidad Carlos III de Madrid, ROR: <https://ror.org/03ths8210>, Department of Aerospace Engineering, Avenida de la Universidad, 30, 28911 Leganés (Madrid), Spain*

²⁾ *Universidad de Málaga, ROR: <https://ror.org/036b2ww28>, Department of Mechanical, Thermal Engineering and Fluid Mechanics, Campus Teatinos, 29010 Málaga, Spain*

(Dated: 15 June 2025)

A 5kW-class, magnetically-shielded Hall effect thruster made of conducting walls is analyzed with a 2D particle/fluid model, in an attempt to understand the trends observed in recent prototypes. Two electrical configurations are considered: floating lateral walls and anode-tied lateral walls. The plasma response in both scenarios is compared with the baseline case of ceramic lateral walls. Under the same operating conditions and magnetic topology, there are minimal changes in performance and in most of the bulk plasma properties for the three cases. The main differences are observed in the electron current and energy flows to the walls in the anode-tied configuration, where the back wall receives only one fourth of the discharge current, and the energy deposition is more uniformly distributed along the walls, as compared with the other two cases, representing a potential advantage from the thermal management perspective. In a subsequent study on the anode-tied configuration, increasing the injected mass flow, up to a factor of four, reduces the energy losses per particle at the wall. At high mass flow operation, there is a large presence of doubly charged ions in the near plume, and the discharge power increases more than proportionally with the injected mass flow, but the thrust efficiency remains invariant.

I. INTRODUCTION

Future space missions demand the development of Hall effect thrusters (HETs) with reduced mass and production costs, as well as extended operation lifetimes. The latter can be achieved through the implementation of magnetic shielding (MS) around the thruster channel walls, which practically eliminates wall erosion as a failure mode in HETs¹. Since this kind of magnetic field topologies drastically reduce plasma-wall interaction, it ~~has been suggested~~ the possibility of replacing traditional dielectric channel walls made of ceramic materials by conducting ones. In general, the latter exhibit (i) improved mechanical and thermo-mechanical properties and (ii) enhanced thermal conductivity and emissivity, which leads to a better thermal management. As a result, they could achieve improved thruster operation, significant mass savings, and higher thruster power density^{2,3}.

In particular, Goebel et al.² have considered graphite channel (or lateral) walls for the H6, a 6 kW MS-HET, with the walls featuring floating (i.e. electrically isolated) conditions. With this configuration, they report only a slight reduction in the total thrust efficiency with respect to the baseline configuration featuring dielectric walls. At the same time, wall temperatures notably decrease when using conducting materials, thanks to their enhanced thermal conductivity and emissivity, which increase heat dissipation from the thruster body. This

paves the way for operating HETs with higher thrust and power densities. In this regard, Hofer et al.³ have extended the previous study to twice the nominal power and to specific impulses up to $I_{sp} \sim 3000$ s with Xe (i.e. a discharge voltage of $V_d \sim 800$ V), using graphite channel walls in the H9C, a 9 kW MS-HET. They report stable operation and are able to maintain high thrust efficiency, of around 60%, when switching V_d from 300 to 800 V (and the discharge power P_d from 9 to 18 kW). In addition to the floating-channel-wall scenario, Hofer et al. have tested conducting channel walls electrically connected to the anode (i.e., anode-tied configuration). All configurations, including floating, anode-tied, and dielectric channel walls, were found to yield nearly indistinguishable performance.

The H9 MUSCLE⁴, a modified version of the H9, with active water-cooling and conducting channel walls, has demonstrated ultrahigh current density operation (up to 10 times greater than nominal) with Xe and Kr at 300 V. The authors observe that, at the highest current density cases, 100% propellant utilization is achieved and the thrust efficiency, although slightly decreased, remains competitive. At this off-nominal operation, Kr is observed to outperform Xe, and the current fraction of doubly-charged ions rises significantly, even surpassing singly-charged ones for Xe. Recently, the H10^{5,6}, a 10 kW-class MS-HET with conducting channel walls and a passive thermal management system, developed based on the experience with the H6 and the H9, has achieved a thrust efficiency peak of 76% with Xe at a discharge voltage of 800V and a discharge power of 10 kW, while operating at high I_{sp} . Moreover, the H10 has shown a

^{a)} Electronic mail: jperales@ing.uc3m.es

significantly large power throttling capability: thrust efficiency was maintained higher than 50% when operating between 3 and 20 kW. Other works, such as Grimaud and Mazouffre^{7,8} and Ding et al.⁹, have demonstrated the feasibility of using conducting channel walls also in low-power MS-HETs, without a significant performance penalty.

Therefore, MS-HETs with conducting lateral walls represent a promising alternative to conventional designs with dielectric channels. This paradigm shift highlights the need for numerical investigations to provide physical insights into the plasma discharge behavior under this new configuration. This work considers a virtual 5 kW-class MS-HET with a centrally-mounted cathode and a geometric and magnetic configuration similar to the one of a real prototype¹⁰, and carries out a numerical investigation of the plasma thruster discharge in three different scenarios: one with dielectric lateral walls and two with conducting lateral walls, floating and electrically connected to the anode. The main goal is to understand to what extent the plasma discharge is affected by the change in the electrical condition of the walls, and to identify potential benefits and drawbacks, in addition to the known mechanical and thermal management improvements with conducting walls. Furthermore, operation at higher-than-nominal current densities is also analyzed as a potential application of MS-HETs with conducting walls. Simulations are carried out with HYPHEN, an axisymmetric hybrid (particle/fluid) code^{11,12}, which has already been used to simulate 5 kW and 20 kW MS-HETs^{10,13}.

The manuscript is structured as follows. Section II briefly introduces the HYPHEN simulation model and presents the simulation set-up, including the virtual thruster geometry and main features. Section III discusses the simulation results for the three cases at nominal operation. Section IV discusses the high-current density operation with conducting walls. Finally, the main conclusions are detailed in Section V.

II. SIMULATION MODEL AND CASES

A 5 kW-class HET with MS topology, similar to the one studied in Ref. 10, is considered in this study. Fig. 1(a) schematically shows the geometry of the thruster and the external region to be simulated. The thruster annular channel has a total length (including the chamfer) $L_c = 2.9$ cm and a radial extension (upstream the chamfer) of 2.22 cm, extending from $r_{in} = 5.45$ cm to $r_{out} = 7.67$ cm. The thruster anode extends along the whole back wall and the cathode is centrally-mounted, around the thruster axis. Both are connected through a power source with a discharge voltage V_d . The reference of the electric potential, $\phi(z, r)$ is taken at the cathode, so the anode potential is V_d . A mass flow rate of xenon neutrals, \dot{m}_A , is injected into the channel through the whole anode wall. The cathode is modeled as a surface

emitting an electron flow equal to the discharge current through the anode-cathode circuit, and a secondary neutral mass flow, \dot{m}_C . The electron and neutral injection conditions are described in detail in Ref. 10.

The exit of the thruster is chamfered, as customarily in MS-HETs¹⁴, to make the walls near-parallel to the local magnetic streamlines, which are represented by the blue lines in Figs. 1(b) and (c). Observe that the magnetic field B features a null point (i.e., $B = 0$) at $z/L_c \approx 0.49$ and close to the channel midline. There is a second magnetic null point along the thruster symmetry axis, in the plume region, which is not important for the analysis here. Fig. 1(d) shows the profile of $B = |B|$ along the thruster channel midline, with a peak of 268 G at $z/L_c \approx 1.2$, while near the anode $B \approx 50$ G.

HYPHEN is a modular code with: an ion (I)-module solving the dynamics of heavy species (neutrals, singly and doubly charged ions) with a particle-in-cell (PIC) formulation; an electron (E)-module solving a quasineutral, drift-diffusive fluid model for the magnetized electrons; and an ancillary sheath (S)-module dealing with the Debye sheaths between the plasma bulk and the different boundaries of the simulation domain, treated as surface discontinuities. The I-module operates on the structured mesh shown in Fig. 1(a) while the E-module works on the magnetic field aligned mesh (MFAM)¹⁵ of Figs. 1(b) and (c), where red lines are magnetic equipotential lines. Mesh interpolation on some plasma magnitudes is thus required. In the simulations presented here, the external region extends slightly more than $6L_c$ for the plume region in the axial direction and slightly less than $6L_c$ in the radial direction. The relevant characteristics of the PIC and MFAM meshes and the timesteps of the simulations are listed in Tab. I.

The I and E-modules solve the quasineutral plasma bulk physics. Zero-thickness Debye sheaths connect the simulated bulk with the different walls and boundaries. All these sheaths are electron-confining, collisionless and unmagnetized, and set the sheath potential fall, $\phi_{WQ} = \phi_Q - \phi_W$, required to collect a net electron current density j_{ne} at the wall:^{10,16}

$$\frac{e\phi_{WQ}}{T_{eQ}} = \ln \left[\frac{en_{eQ}\bar{c}_{eQ}}{-4j_{ne}} \sigma_{rp}(1 - \delta_s)(1 - \delta_r) \right]. \quad (1)$$

Here Q represents the sheath edge (and boundary of the quasineutral plasma domain), W represents the wall, n_e is the electron density, T_e the electron temperature, $\bar{c}_e = \sqrt{8T_e/\pi m_e}$, $\delta_s(T_{eQ})$ is the secondary electron emission (SEE) yield, $\delta_r(T_{eQ})$ is the fraction of primary electrons being elastically reflected by the wall, and σ_{rp} is the thermalization fraction of primary electrons collected by the wall. These sheaths do not impose any control on the ion current impacting the wall, j_{ni} .

Figure 1(a) shows the different surfaces we are considering for the simulations. The magenta line identifies the symmetry axis. The green line at the channel back wall is the metallic anode and the main injector of neutrals. The small black box represents the centrally-

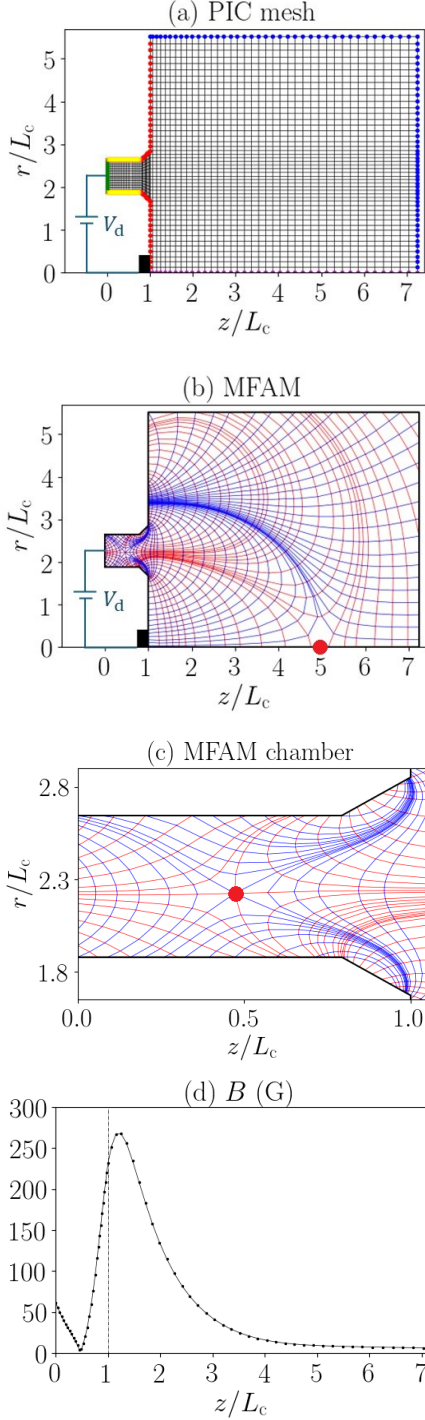


FIG. 1. (a) PIC mesh, (b) MFAM, (c) detail of the MFAM within the thruster chamber, and (d) magnitude of \mathbf{B} along the thruster chamber midline. In (a), boundary types are identified by colors: in green the anode wall; in yellow the channel lateral walls (i.e. dielectric or conducting); in red the external dielectric walls; in blue the downstream plume boundary, P. In (b)-(c), blue and red lines are \mathbf{B} -parallel and \mathbf{B} -perpendicular lines, respectively, and red dots are singular (i.e. null) points of the magnetic lines.

Simulation parameter	Units	Value
PIC mesh number of cells, nodes	-	3243, 3360
PIC mesh smallest grid size	mm	1
MFAM number of cells, faces	-	2030, 4171
MFAM average skewness ¹⁷	-	0.059
Ion-moving timestep, Δt	ns	15
Total number of simulation steps	-	60000

TABLE I. Main simulation parameters and mesh characteristics.

mounted cathode, injecting neutrals and electrons. The red lines, covering the chamfer and the external walls of the thruster, are considered dielectric in all cases. The blue lines are the downstream plume boundary P, where the global electric current is assumed zero, corresponding to a current-free plume.

Then, the yellow lines represent the channel lateral walls, for which three cases are considered:

1. in case D, these walls are made of Boron-Nitride (BN), with dielectric properties;
2. in case F, each wall (i.e. inner and outer) is conducting and floating;
3. in case T, each wall is again conducting but electrically tied to the anode.

At dielectric walls a local zero-current condition $j_n = \mathbf{j} \cdot \mathbf{1}_n = 0$ is applied with \mathbf{j} the electric current density and $\mathbf{1}_n$ the normal-to-wall vector, pointing out of the domain. This condition determines the potential fall at the sheath, and thus the local wall potential. Secondary electron emission by electron impact is included only at dielectric walls and contributes to j_n ¹⁰.

At a floating conducting wall, with area S_L , the zero-current condition is

$$\int_{S_L} j_n dS = 0, \quad (2)$$

and determines the global wall potential, the local current density j_n , and the local sheath potential fall.

For cases D and F, at the current-driving anode, with area S_A , we have

$$\int_{S_A} j_n dS = I_d, \quad (3)$$

with $j_n = j_{ni} - j_{ne}$. Since the anode potential is V_d , this condition determines the discharge current I_d . For case T, Eq. (3) is applied to the whole area of anode plus lateral conducting walls. Finally, at the plume boundary, the global zero-current Eq. (2) is applied for the plume boundary area S_P ¹⁸.

In HYPHEN, the PIC and fluid formulations require empirically-fitted models for (a) plasma-wall interaction

parameters (such as energy accommodation of heavy species impacting walls and secondary electron emission) and (b) the electron anomalous cross-field transport. We will take a unique fitting for the three cases here. In the case of wall interaction parameters, the sensitivity of the results to them has been found small, due to the MS configuration of the thruster¹⁹.

For the electron anomalous transport, we consider the widely used model based on the assumption that there is an additional azimuthal force due to nonlinear azimuthal instabilities, which, once averaged over azimuth and high frequencies, can be expressed as $\alpha_t(z)\omega_{ce}m_e u_{\theta e}$, with $\omega_{ce} = eB/m_e$ and $u_{\theta e}$ the azimuthal electron velocity. As in Refs. 10 and 13 we opt for a step profile of α_t , with α_{t1} and α_{t2} applied in, approximately, the thruster chamber and the near plume regions, respectively. While the different configurations of the channel walls may induce changes in the electron anomalous transport, the operation of the H9C prototype with dielectric and conducting walls has exhibited negligible differences in the discharge current mean value and similar amplitude and frequency content of the discharge current oscillations³. This evidence is used here to keep the same α_{t1} and α_{t2} for the three simulation cases.

III. COMPARISON OF THE THREE CASES

Cases D, F and T are simulated for the same operational conditions: the magnetic topology described in Sec. II, $V_d = 300$ V and a total mass flow of $\dot{m} = 15.05$ mg/s, with 7% (i.e. 1.05 mg/s) emitted by the cathode. Turbulent transport parameters were adjusted ($\alpha_{t1} = 0.7\%$ and $\alpha_{t2} = 4\%$) to retrieve I_d and F values similar to the experimental ones from Ref. 10 for the same operation point and dielectric walls. The rest of parameters are as in Ref. 10. The number of simulated timesteps is 60000 (900 μ s of simulation time), enough to capture several low-frequency (i.e. breathing mode) oscillation cycles of I_d . The results presented in the following sections are time-averaged over several of these breathing mode cycles.

A. 2D maps

Figure 2 depicts, for cases D, F and T, the time-averaged 2D maps inside the thruster channel of the main plasma variables. The three cases exhibit the usual features of a MS-HET plasma discharge^{1,10}: the profiles of ϕ and n_e (first and third rows, respectively) are rather uniform inside the channel, placing most of the ion acceleration and beam expansion at the channel exit; T_e , [Figs. 2(d)-(f)] is low inside the channel, specially at the walls, and follows closely the magnetic lines, unlike ϕ ; ions are practically unmagnetized and, with low inertia, they follow the local electric field, which explains the ample region with backward ion flow and the flows to the

lateral walls [in Figs. 2(j)-(l)]; electrons are highly magnetized and they are channeled across the magnetic null point inside the chamber [in Figs. 2(m)-(o)].

The comparison among the cases D, F and T shows that the 2D maps are nearly identical for all the magnitudes, except for: (i) the electric potential ϕ , which uniformly rises around 4 V in case T [Fig. 2(c)] with respect to cases C and F [Figs. 2(a) and (b)], with very slight changes in the gradients; and (ii) the maps of \tilde{j}_e (and thus \tilde{j}). Here, \tilde{j}_e , \tilde{j}_i , and \tilde{j} represent longitudinal currents, once the azimuthal components are subtracted. The azimuthal electron current, $j_{\theta e}$, not plotted here and driver of the magnetic thrust ($\propto j_{\theta e} B_r$), is found to be similar for the three cases; the azimuthal ion current is negligible. Figs. 2(m)-(o) reveal similar \tilde{j}_e maps in the plasma bulk (in both magnitude and direction) for cases D and F, due to the fact that in both scenarios the net electric current collected at the lateral walls is null. The null local current condition imposed at the dielectric channel walls in case D yields \tilde{j} streamlines parallel to the walls in Fig. 2(p). On the other hand, the floating condition in case F permits the electric current density to flow locally from the plasma to the channel walls and vice versa, with \tilde{j} locally intersecting the channel walls in the corresponding directions [refer to Fig. 2(q)], so that the net collected current is null.

Upstream the B null point, case T exhibits a notably different \tilde{j}_e map with respect to cases D and F, as depicted in Fig. 2(o). Differences are induced by the change in the boundary condition imposed at the channel walls: unlike in cases D and F, the anode-tied conducting channel walls in case T can collect a certain net electric current (i.e., a fraction of I_d), thus decoupling ion and electron currents collected at the channel walls. While the unmagnetized ion current solution is practically unaffected, a large fraction of electrons is redirected towards the lateral channel walls along the B lines around the separatrices, which cross the magnetic null point [refer to Fig. 1(c)], where electrons are unmagnetized and can easily move across magnetic tubes. This implies that \tilde{j}_e be redistributed from the B null point (according to the different electrical conditions of the channel walls) without a significant change in ϕ and n_e gradients. These results highlight the central role of the B topology and, in particular, the relevance of the presence and location of the magnetic null point for the electron current solution inside the chamber.

B. Wall profiles

Figure 3 shows, for cases D (black line), F (red line) and T (green line), the profiles along the thruster chamber walls, excluding the chamfers, of relevant plasma variables. In agreement with Fig. 2, the electron densities and temperatures at the sheath edge [in Fig. 3(a) and (b), respectively] and the ion current to the walls [in Fig. 3(e)] are very similar for the three cases. Differences

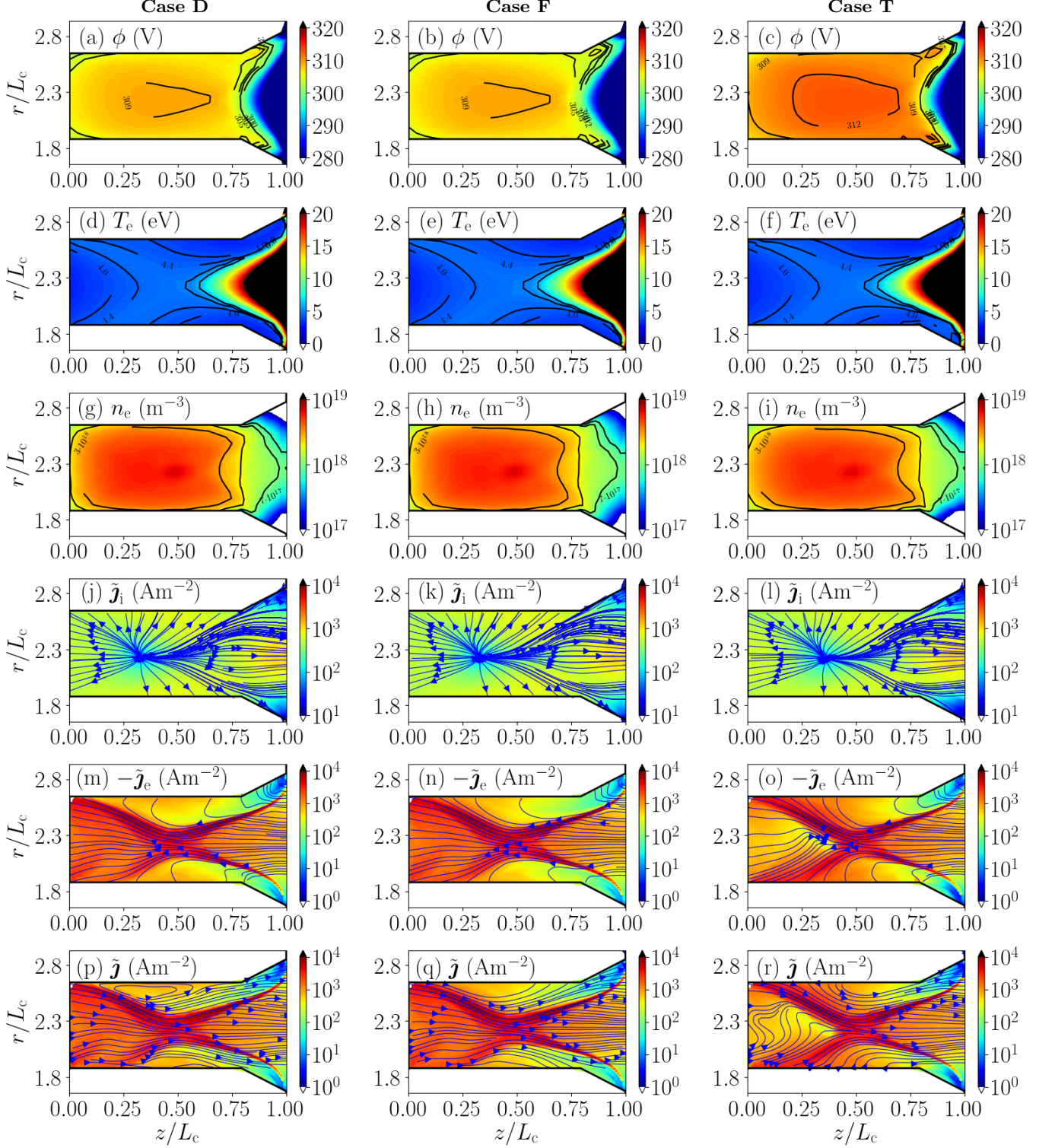


FIG. 2. Time-averaged 2D(z, r) contour maps inside the thruster chamber for Case D (first column), F (second column) and T (third column). (a)-(c) Electric potential ϕ , (d)-(f) electron temperature T_e , (g)-(i) plasma density, n_e , (j)-(l) in-plane ion current density \tilde{J}_i , (m)-(o) in-plane electron current density \tilde{J}_e and (p)-(r) in-plane electric current \tilde{J} . Blue lines with arrows indicate streamlines of \tilde{J}_i , $-\tilde{J}_e$ and \tilde{J} , respectively.

are found in the electron currents to the wall, the local potentials at the wall and sheath edge (ϕ_W and ϕ_Q , respectively) and the magnitudes related to them. In Fig. 3(c), for case D, ϕ_W is minimum at the anode corners and then increases along inner and outer dielectric walls, and it even gets close to V_d downstream. For case F, to collect a null total electric current, ϕ_W at the inner and outer floating walls is 7 V and 6.4 V, respectively, below the anode potential. Regarding ϕ_Q along the walls, again in Fig. 3(c), it is practically the same for cases D and F, while for case T the profile remains practically unaltered, but shifted up 3 V approximately. This increase in ϕ_Q is caused by the higher $\Delta\phi_{WQ}$ found at the anode [see Fig. 3(d)] to reduce the electron current collected there [refer to Fig. 3(e)]. Also, it leads to the higher electric potential in the plasma bulk for case T observed in Fig. 2(c). Additionally, the increase in ϕ_Q is small enough so that $\Delta\phi_{WQ}$ becomes lower along the lateral channel walls (compared to cases D and F), allowing a larger amount of \tilde{j}_e to be collected at those surfaces.

Following Eq. (1), the shape of $\Delta\phi_{WQ}(s)$ adjusts itself to control the profile of $j_{ne}(s)$, in Fig. 3(d). In Case D, along the dielectric lateral walls, $j_{ne}(s)$ equals $j_{ni}(s)$, and thus $j_{ne}(s)$ is determined by the plasma bulk response only. In Case F, the balance of ion and electron currents in the lateral channel walls is satisfied globally, which lies a certain excess of j_{ne} near the anode and a defect near the exit, driven by the local plasma properties. In case T, as it was pointed before, a fraction of the electron current collected by the anode in cases D and F is now collected by the lateral channel walls. For this reason, the profile of j_{ne} along the chamber walls in case T differs significantly from the other two cases. Regarding j_{ni} , at the lateral channel walls, the collected ion current is practically the same among cases, while a slight increase is found at the anode wall for case T.

Continuing with Fig. 3(f), $\mathcal{E}_{iW} = P''_{niW}/j_{ni}$ is the average energy per unit of ion current reaching the walls and is equal to $e\Delta\phi_{WQ}$ plus the small energy gained in the plasma bulk, as the plots illustrate. The differences among \mathcal{E}_{iW} profiles shown in Fig. 3(f) are mostly determined by changes in $\Delta\phi_{WQ}$ [see Fig. 3(d)], since the gradients of ϕ within the plasma bulk barely change from one case to the other [Figs. 2(a)-(c)]. Among the three scenarios, case T exhibits the largest \mathcal{E}_{iW} at the anode wall, while case F does so at the channel walls. The values of \mathcal{E}_{iW} are below the usual thresholds for wall erosion^{20,21}, which confirm that walls remain nearly erosion-free in the three configurations. \mathcal{E}_{eW} is the average impact energy per net wall-collected electron, which, in our model, is equal to $2T_{eQ}$ if there is no SEE (i.e. in our conducting walls), and is larger with SEE (due just to averaging on the net electron current). Given the similar T_{eQ} solution for all cases [see Fig. 3(b)], the main differences on \mathcal{E}_{eW} profiles are due to the SEE, which only exists in case D along the dielectric channel walls. Nonetheless, the low values of T_{eQ} imply low SEE yields ($\delta_s \approx 15\%$) and leads to only a moderate increase (of at most about 25%) in

\mathcal{E}_{eW} in case D.

Figures 3(g), (h), and (i) show the plasma energy flux to the walls, defined as $P''_{nW} = (j_{ni}\mathcal{E}_{iW} - j_{ne}\mathcal{E}_{eW})/e$, and the contributions from ions, P''_{niW} , and electrons, P''_{neW} . For cases D and F, since $\mathcal{E}_{eW} < \mathcal{E}_{iW}$ and ion and electron currents are similar (or equal), it follows that $P''_{neW} < P''_{niW}$ along most of each lateral wall. At the anode wall, the larger j_{ne} yields $P''_{neW} > P''_{niW}$, since ion and electron impact energies are similar. For case T, the P''_{neW} profile closely follows the j_{ne} profile: it increases at the channel walls and decreases at the anode wall with respect to cases D and F. As for ions, the opposite behavior is found, and P''_{niW} decreases at the channel walls and increases at the anode wall. As a result, P''_{nW} has a more uniform behavior in case T than in the other two cases. The integration along the anode and lateral walls of j_{ni} , j_{ne} , and P''_{nW} constitutes some of the global magnitudes discussed next.

C. Global performances

Once the 2D plasma response has been analyzed for the three cases, we can obtain integral magnitudes that characterize the global differences among them. Current and power balances are essential elements for this comparison. In steady state, they can be expressed as

$$I_{prod} - I_{iP} = I_{iL} + I_{iA} + I_{iC} = I_{eL} + I_{eA} - |I_{eC}| \quad (4)$$

and

$$P = P_P + P_L + P_A + P_{inel}. \quad (5)$$

In Eq. (4), I_{prod} is the total ion/electron current generated by ionization in the simulation domain, formally defined as

$$I_{prod} = e \int_{\Omega_p} (\dot{n}_{01} + 2\dot{n}_{02} + \dot{n}_{12}) d\Omega, \quad (6)$$

with $n_e = n_{i1} + 2n_{i2}$ the electron or plasma density, n_{i1} and n_{i2} the densities of Xe^+ and Xe^{2+} , $\dot{n}_{01} = n_e n_n R_{01}$, $\dot{n}_{02} = n_e n_n R_{02}$, and $\dot{n}_{12} = n_e n_{i1} R_{12}$ the production sources, and $R_{01}(T_e)$, $R_{02}(T_e)$, and $R_{12}(T_e)$ the ionization rates for processes $Xe+e \rightarrow Xe^++2e$, $Xe+e \rightarrow Xe^{2+}+3e$, and $Xe^++e \rightarrow Xe^{2+}+2e$, respectively.

Also in Eq. (4), I_{iP} is the ion (and electron) beam current leaving the domain through the current-free plume boundary [blue line in Fig. 1(a)]; I_{iL} and I_{eL} are the ion and electron currents collected at the thruster lateral and external walls [i.e., the yellow and red walls in Fig. 1(a)]; I_{iA} and I_{eA} the ion and electron currents collected at the anode [green wall in Fig. 1(a)]; $-|I_{eC}|$ is the current emitted by the cathode, and I_{iC} the ion current collected by the cathode, which is negligible. All currents are considered positive when the corresponding particles are collected by the wall. Thus: $I_L = I_{eL} - I_{iL}$ is the net current collected at the channel walls, different from

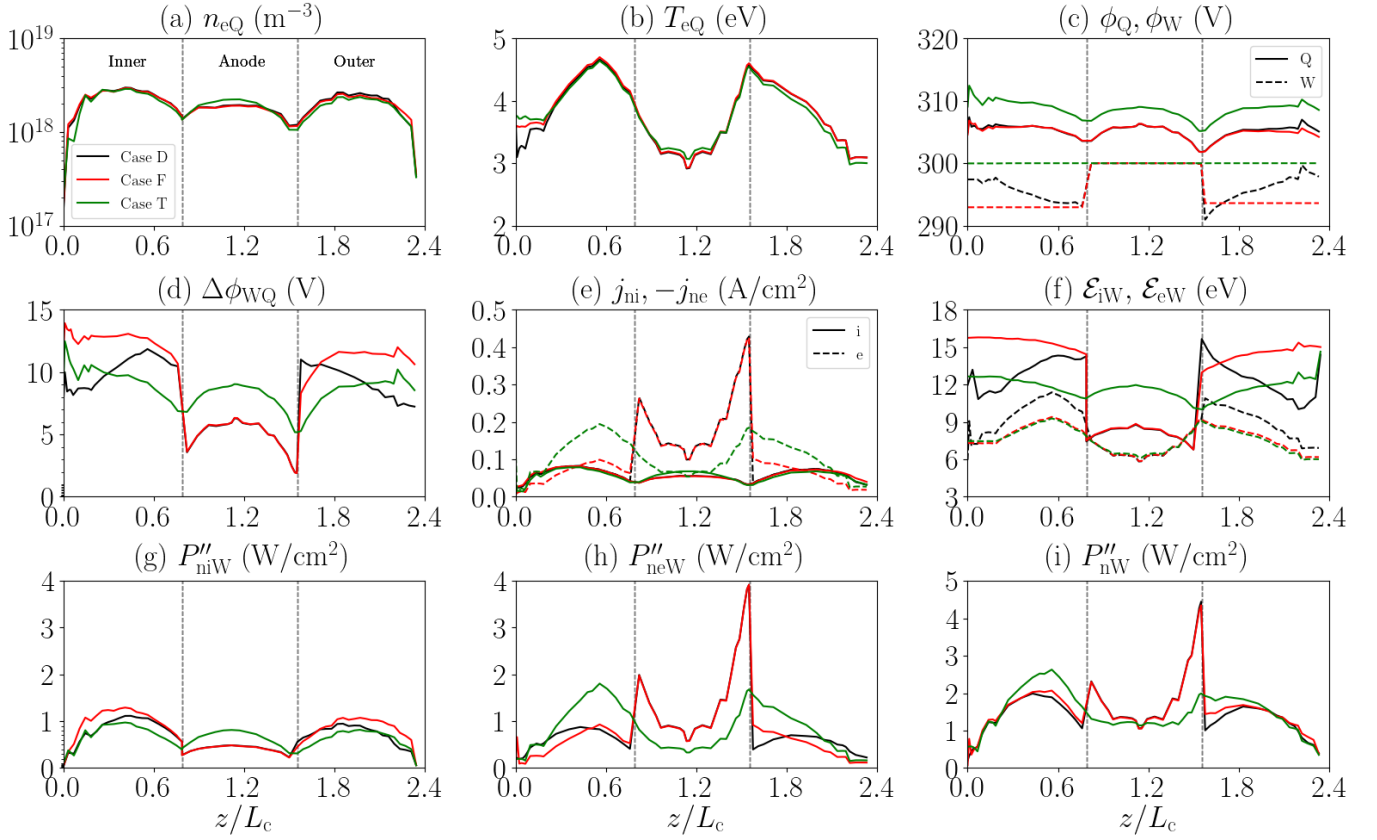


FIG. 3. Time-averaged profiles of main plasma magnitudes along the thruster channel and anode walls [yellow and green boundaries in Fig. 1(a)] for case D (black lines), case F (red lines) and case T (green lines). Coordinate s runs from the outermost end of the inner channel wall to the outermost end of the outer channel wall. Subindex W refers indistinctly to lateral walls and anode.

Case	F (mN)	I_d (A)	I_{prod} (A)	I_{iP} (A)	I_{iL} (A)	I_{eL} (A)	I_{iA} (A)	I_{eA} (A)	P (W)	P_P (W)	P_{inel} (W)	P_{iL} (W)	P_{eL} (W)	P_{iA} (W)	P_{eA} (W)
D	257	14.0	28.6	11.8	12.6	12.6	4.1	18.3	4225	3170	553	177	156	34	135
F	257	13.9	28.6	11.7	12.8	12.8	4.0	18.0	4180	3114	556	205	138	33	134
T	255	14.0	28.1	11.7	11.7	22.2	4.7	8.2	4187	3155	536	163	222	54	57

TABLE II. Thrust, main plasma currents and contributions to the ion and electron current balances in Eq. (4). The tiny $I_{iC} \approx 0.3\%$ of I_{prod} has been omitted. Discharge power and contributions to the plasma energy balance in Eq. (5).

zero only for case T; $I_A = I_{eA} - I_{iA}$ is the net current collected at the anode wall; and the discharge current is $I_d = I_A + I_L = |I_{eC}| + I_{iC}$. In general, both I_{iC} and the contribution of external walls to I_{iL} and I_{eL} can be neglected.

In Eq. (5): $P = I_d V_d + P_C$ is the input power, which includes a tiny contribution ($P_C \sim 1\%$) from the injected electron energy at the cathode; P_P is the plasma energy flow across the plume boundary; and P_A and P_L are plasma energy flows at, respectively, the anode and the rest of thruster walls [with a negligible contribution from the thruster external walls, red boundary in Fig. 1(a)]; and

$$P_{inel} = P_{prod} + P_{exc} \quad (7)$$

is the energy loss due to inelastic (ionization and excitation) collisions on the whole simulation domain, constituted of

$$P_{prod} = \int_{\Omega_p} [\dot{n}_{01}\mathcal{E}_{01} + \dot{n}_{02}\mathcal{E}_{02} + \dot{n}_{12}(\mathcal{E}_{02} - \mathcal{E}_{01})] d\Omega, \quad (8)$$

the ionization or plasma production losses, with $\mathcal{E}_{01} = 12.1$ eV and $\mathcal{E}_{02} = 33.3$ eV for xenon, and

$$P_{exc} = \int_{\Omega_p} n_e n_n \sum_k R_k(T_e) \mathcal{E}_k d\Omega, \quad (9)$$

the excitation losses due to e-n excitation of multiple states of Xe, followed by radiative deexcitation.

Table II presents the main performance figures and main contributions to the currents and powers of Eqs. (4) and (5). The very similar plasma responses for the three cases imply that overall performance figures are barely affected by the change in the wall properties and electrical configuration of the channel walls, in agreement with previous experimental works^{2,3,7}. The range of variation of the main performance metrics for the three cases under analysis is $I_d = [13.9 \text{ A}, 14.0 \text{ A}]$, $F = [255 \text{ mN}, 257 \text{ mN}]$, $P = [4.18 \text{ kW}, 4.22 \text{ kW}]$, and $\eta = F^2/(2\dot{m}P)=[51.6\%, 52.0\%]$.

Results confirm a similar distribution of the electron current to the different thruster chamber walls in cases D and F. However, case T exhibits a deficit of around 10 A (a 34% in terms of I_{eA}/I_{prod}) with respect to the other two cases, which is compensated by a similar increase in I_{eL}/I_{prod} . The terms of the ion current balance I_{iL}/I_{prod} and I_{iA}/I_{prod} , in Tab. II, vary only slightly from cases D and F to case T. These ion current variations ($\sim 3\%$ of I_{prod}) are caused by small changes in the gradients of ϕ , required to redistribute I_e among the thruster walls. In case T, the fraction of I_d that flows through the lateral channel walls, I_L/I_d , is approximately 75% (of which a 51.9% goes to the inner wall, and a 48.1% to the outer one). The net current collected there is mainly driven by electrons. The slightly larger ion current to the anode contributes to reduce the fraction of I_d collected at the anode wall. In Ref. 3, experimental observations for the H9C thruster in anode-tied configuration yield $I_L/I_d = 33 - 40\%$. Unlike the MS-HET simulated here, the H9C features a MS topology without ***B* null point** inside the thruster chamber²². Differences in the magnetic topology and the geometry could be postulated as the main reasons for the different fractions of I_d collected at the conducting channel walls.

Case T exhibits a 33% relative decrease of the power deposited in the anode wall P_A ($= 111 \text{ W}$) with respect to cases D and F ($\approx 168 \text{ W}$), which is mainly driven by the lower electron current fraction to the anode wall. Reducing the heat load to the anode can help keep its temperature at nominal operating conditions, without the need of complex active cooling systems which can pose severe restrictions for practical operation²³. The lower P_A implies higher P_L in case T ($= 385 \text{ W}$), with respect to cases D ($= 333 \text{ W}$) and F ($= 343 \text{ W}$). Apart from potential advantages thanks to the extra thermal conductivity obtained from electrically/thermally connecting the anode and the conducting channel walls³, the observed redistribution of heat loads to the thruster surfaces may be beneficial for thermal management, because thermal paths towards radiative surfaces can be shorter from the channel walls than from the anode (i.e., it is in general easier to evacuate P_L than P_A).

IV. HIGH CURRENT DENSITY OPERATION

Experimental evidence supports that conducting walls enable MS-HET to operate at higher-than-nominal current densities, leading to thrust density levels previously unattainable with HETs⁴. This section numerically investigates the increase of the current density for the previous T configuration, considering mass flow rates $\dot{m} = f \times (15.05 \text{ mg/s})$, with $f = 1, 2$ and 4. The rest of the parameters in the simulations remain unchanged.

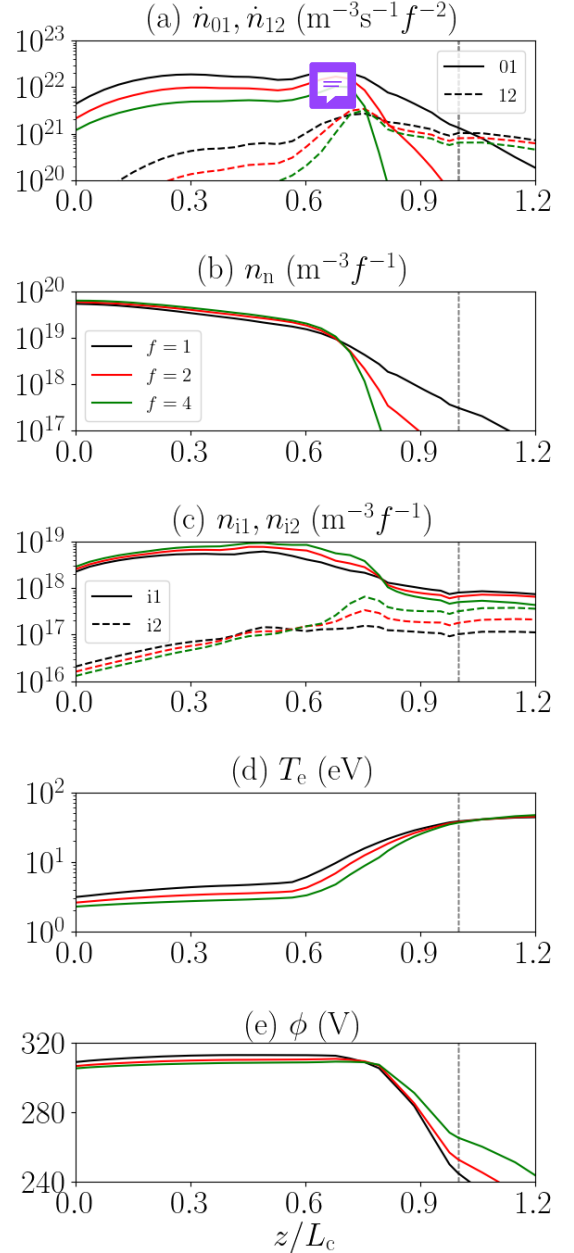


FIG. 4. Time-averaged axial profiles of main plasma magnitudes along the thruster channel midline for case T: nominal case (black line), with twice the input mass flow (red line), and four times the input mass flow (green line).

f	F/f (mN)	I_d/f (A)	I_{prod}/f (A)	I_{1P}/f (A)	I_{2P}/f (A)	I_{1W}/f (A)	I_{eW}/f (A)	P/f (kW)	P_P/f (kW)	P_{zP}/f (kW)	P_{inel}/f (kW)	P_{1W}/f (kW)	P_{eW}/f (kW)	η_u	η
0.5	227	11.9	22.9	8.5	1.7	13.0	25.2	3.57	2.69	2.29	0.36	0.22	0.30	0.84	0.48
1	255	14.0	28.1	8.6	3.1	16.4	30.4	4.20	3.16	2.65	0.54	0.21	0.28	0.92	0.52
2	276	15.8	32.3	8.0	5.2	18.8	34.9	4.70	3.56	2.92	0.68	0.20	0.26	0.96	0.53
4	298	18.3	37.8	6.5	9.0	21.1	40.1	5.42	4.11	3.25	0.87	0.19	0.25	0.99	0.52

TABLE III. Mass flow sensitivity study. All extensive magnitudes are shown normalized by f . I_{1P} and I_{2P} are the downstream currents of singly and doubly charged ions. P_{zP} is the downstream flow of axial plasma energy.

Figure 4 compares time-averaged axial profiles of relevant plasma magnitudes at the chamber mid-radius for the three cases. Since species densities scale primarily with \dot{m} , they have been normalized by f to enable a more precise comparison among cases. The ionization rates, which are proportional to the square of the densities, have been scaled with f^2 . The five magnitudes shown in the figure are strongly interrelated. From Fig. 4(a), production of Xe^+ starts at the anode region, is maximum at $z/L_c \approx 0.7$ and then decays sharply as the neutrals [see Fig. 4(b)] are depleted. Production of Xe^{++} is almost exclusively due to \dot{n}_{12} , since R_{02}/R_{01} is very negligible (below 0.01) for the range of T_e found inside the thruster. It becomes relevant once the production of Xe^+ is nearly complete, and reaches a maximum at $z/L_c \approx 0.75$. Downstream this point, it decays gradually as n_{i1} decreases, coinciding with the acceleration of Xe^+ ions by the potential drop [refer to Fig. 4(e)]. Both ϕ and T_e exhibit a plateau along the first half of the channel, followed by steep gradients near the channel exit.

Figure 4 compares case $f = 4$ with case $f = 1$, highlighting the following key features. The neutral depletion [Fig. 4(b)] is almost complete and takes place in a shorter region due to the dependence of \dot{n}_{01} on f^2 . The electron temperature [Fig. 4(d)] is similar at the thruster exit [$T_e \approx 37$ eV], but it is smaller inside the chamber due to higher inelastic losses per unit of mass, as we will further see below. This decrease of T_e explains that ionization sources, depending exponentially on T_e , do not scale so well with f^2 in Fig. 4(a). The normalized neutral density at the anode, n_{nA}/f , increases about a 16%, due to a higher back flow (and thus anode recombination) of ions. Indeed, there is a higher production of Xe^+ , so that, up to $z/L_c \approx 0.70$, $n_e/f \simeq n_{i1}/f$ is about a 30% higher.

Table III quantifies main performance parameters for $f = 1, 2$, and 4; the case $f = 0.5$ is added to complete the analysis that follows. All extensive magnitudes have been normalized by f . Since anode and lateral walls are both conducting and at the same electric potential, we group contributions of both walls under subindex W. Let us focus again on the comparison of cases $f = 1$ and $f = 4$. First, the normalized downstream mass flow of ions, \dot{m}_{iP}/f [with $\dot{m}_{iP} = (m_i/e)(I_{1P} + I_{2P}/2)$], increases an 8% until reaching almost total ionization (including the 7% of cathode mass flow): propellant utilization, $\eta_u = \dot{m}_{iP}/\dot{m}$, is 92% and 99% for $f = 1$ and 4, respectively.

With almost total depletion of neutrals, the production of Xe^{++} increases notably from $f = 1$ to 4: the relative downstream mass flow of Xe^{++} goes from $\dot{m}_{i2P}/\dot{m} = m_i I_{i2P}/(2e\dot{m}) \approx 14\%$ to 40%; and Xe^{++} contribution to the downstream ion current, $I_{iP} = I_{1P} + I_{2P}$, goes from a 26% to a 58%. The larger contribution of Xe^{++} to the electric current justifies that normalized ion currents, I_{prod}/f and I_{iP}/f , increase by 35 %. The normalized ion and electron currents to the lateral walls and anode increase about 29-32%, in agreement with the increase on n_e/f reported above. The normalized discharge current I_d/f and thus the discharge power increases about a 30%. This means that the current efficiency, $\eta_{\text{cur}} = I_{iP}/I_d$, a contributor to the thrust efficiency, increases from 82% to 85%.

The distribution of the increment of P_d/f among the different terms in the power balance [Eq. (5)], is however dissimilar: P_P/f increases by 30% too, but $(P_{1W} + P_{eW})/f$ decreases by 8% and P_{inel}/f increases by 61%. Since P_{inel} affects T_e in the electron energy balance, the increase in P_{inel}/f with f explains, on the one hand, the associated decrease of T_e inside the thruster observed in the previous figure. On the other hand, this increase in P_{inel}/f is caused by the 37% extra cost of producing one Xe^{++} instead of two Xe^+ , as well as by the augmented fraction of excitation losses as T_e decreases: $P_{\text{exc}}/P_{\text{inel}}$ is 51% and 60% for $f = 1$ and 4, respectively. The ratio P_{1W}/I_{iW} provides an estimate of the average energy loss per (effective) singly-charged ion impacting at a thruster wall. This ratio decreases from 12.1 eV to 9 eV with f increasing from 1 to 4, which is favorable in terms of wall erosion, and is explained by the decrease in T_e . Finally, looking at the thrust and specific impulse, F/\dot{m} and $I_{sp} = F/\dot{m}$, both increase by 17%, which means $\approx 35\%$ increase of $(F/f)^2$ and a practically invariable thrust efficiency, $\eta = 52\text{-}53\%$.

The case $f = 2$ is just an intermediate state in the evolution of the discharge from $f = 1$ to 4, and serves to confirm that the above trends are robust. Instead, comparing the low-mass flow case $f = 0.5$ with $f = 1$, Tab. III shows a penalization of 4 absolute points in the thrust efficiency, due mainly to the degradation in propellant utilization, which decreases from 92% to 84%. For $f = 0.5$, the presence of doubly-charged ions in the beam is below a 10%. Therefore, as f increases towards 1, we improve the thrust efficiency mainly by increasing

mass utilization via single-charge ionization. Once in the high-current regime (say $f > 1$), the discharge achieves near-total ionization and this favors a much higher production of doubly-charged ions. This yields, along with an augmented fraction of excitation losses, a penalization on normalized inelastic losses, but it is compensated by a lower contribution of wall losses, keeping the thrust efficiency almost unaltered. In terms of partial efficiencies, the improvement of η_u and η_{cur} with f is nearly canceled by a larger plume divergence: P_{zP}/P_P , which measures the energy penalty by plume divergence, decreases from 84% to 79% when f goes from 1 to 4 (refer to Tab. III). Two additional benefits of high thrust density operation are the increase of specific impulse and the reduction of the ion impact energy.

These results from a theoretical/numerical analysis are well aligned with existing experimental evidence. In particular, Ref. 4 reports a similar behavior in terms of: (i) the enhancement of η_u , which reaches 100%; (ii) the increased presence of Xe^{++} under high current density operation of the H9 MUSCLE; (iii) the increase in plume divergence; and (iv) the minimal degradation in performance. A last observation is that our analysis has kept invariable the parameters of turbulent transport with f . This is partially supported by recent works²⁴ suggesting the independence of anomalous transport on n_e , but only a direct comparison of the simulations with experimental results would validate our assumption.

V. CONCLUSIONS

A virtual 5 kW MS-HET with conducting channel walls is analyzed with an axisymmetric particle/fluid model and compared to the case of a conventional chamber with a metallic anode and ceramic lateral walls (case D). In turn, the case with conducting channel walls is studied with two electrical configurations, one where the lateral walls are floating (case F) and the other extending the anode to the entire chamber (case T).

The comparison of the three cases shows that the magnetic shielding is effective in all of them. There are only minimal differences in thruster performances and the 2D maps of relevant plasma magnitudes, such as densities of the several species, the electron temperature, and the ion current streamlines. The electric potential map and the electron current streamlines inside the chamber are the most affected by the change in wall conditions. Yet, variations in the electron streamlines between cases D and F, both with no electric current collected by the lateral walls, are minimal.

In this context, case T, with all chamber walls acting as anode, is the most interesting one. Here, the back wall collects only 25% of I_d , with the electron current being redistributed with respect to the other two cases around the magnetic null point (thus with minimal changes in the electric potential gradients) and yielding a more uniform distribution of the energy fluxes to the thruster walls with

lower heat loads to the anode and higher ones to the channel walls. This fact and the better thermal properties of conducting materials are beneficial for thruster thermal management.

The good performance of the case T has motivated the second part of the study, where high-current (i.e., high power) operation has been analyzed by increasing up to 4 times the injected mass flow, without modifying the magnetic topology and the discharge voltage. Although in first approximation the increase of all the extensive magnitudes is proportional to that of the mass flow, there is an additional variation caused by a different composition of the heavy species in the plasma. For example, by multiplying the mass flow rate by four, the discharge power is multiplied by 5, going from 4.2 kW to 22 kW. This is because the nominal case has already achieved high propellant utilization, and increasing the mass flow rate boosts the presence of doubly-charged ions and thus the required discharge current. Doubly-charged ions lead, along with an augmented fraction of excitation losses at lower electron temperature, to higher relative inelastic energy losses, but this is compensated by lower relative wall energy losses. In summary, the thrust efficiency remains almost unchanged between 4.2 and 22 kW, the specific impulse increases by a 17%, and the magnetic shielding continues to be effective, thus keeping the ion impact energy very low.

Due to the large presence of doubly-charged ions at high-current operation, further studies should consider the amount and influence of triply-charged ions and benefits for possible adjustment of the magnetic topology (e.g., the location of the null point). The analysis of all cases has been made without modifying the parameters of empirical models for wall interaction and turbulent transport. Although there is indirect experimental support for proceeding that way, only the simulation of real cases will shed more light on this.

ACKNOWLEDGMENTS

This work has been supported by the project HEEP, funded by Agencia Estatal de Investigación (AEI), under Grant Agreement MCIN/AEI/10.13039/501100011033 and by “ERDF A way of making Europe”, under Grant Agreement PID2022-140035OB-I00. A first version of this work was presented at the 38th International Electric Propulsion Conference²⁵.

CONFLICT OF INTEREST

The authors have no conflicts to disclose

REFERENCES

- ¹I. G. Mikellides, I. Katz, R. R. Hofer, and D. M. Goebel, "Magnetic shielding of a laboratory Hall thruster. I. Theory and validation," *Journal of Applied Physics*, vol. 115, no. 4, p. 043303, 2014.
- ²D. M. Goebel, R. R. Hofer, I. G. Mikellides, I. Katz, J. E. Polk, and B. N. Dotson, "Conducting wall Hall thrusters," *IEEE Transactions on Plasma Science*, vol. 43, no. 1, pp. 118–126, 2015.
- ³R. Hofer and S. Arestie, "Performance of a conducting wall, magnetically shielded Hall thruster at 3000s specific impulse," in *37th International Electric Propulsion Conference*, ser. IEPC-2022-401, 2022.
- ⁴I. Su, T. Gill, P. Roberts, W. Hurley, T. Marks, C. Sercel, M. Allen, C. Whittaker, M. Byrne, Z. Brown, E. Vigas, and B. Jorns, "Operation and performance of a magnetically shielded Hall thruster at ultrahigh current densities on xenon and krypton," in *AIAA SCITECH 2023 Forum*. National Harbor, MD: AIAA, 2023.
- ⁵R. Hofer, J. Simmonds, G. D., J. Steinkraus, and A. Paymann, "The H10 high power density Hall thruster," in *38th International Electric Propulsion Conference*, no. IEPC-2024-515. Toulouse, France: Electric Rocket Propulsion Society, Fairview Park, OH, 2024.
- ⁶J. Simmonds, R. Hofer, S. Firdosy, T. Daimary, E. Smith, S. Roberts, T. Wexler, P. Dillon, and G. D., "Thermal management and krypton performance of the H10 high power density Hall thruster," in *38th International Electric Propulsion Conference*, no. IEPC-2024-257. Toulouse, France: Electric Rocket Propulsion Society, Fairview Park, OH, 2024.
- ⁷L. Grimaud and S. Mazouffre, "Conducting wall Hall thrusters in magnetic shielding and standard configurations," *Journal of Applied Physics*, vol. 122, no. 3, 2017.
- ⁸—, "Performance comparison between standard and magnetically shielded 200W Hall thrusters with BN-SiO₂ and graphite channel walls," *Vacuum*, vol. 155, pp. 514–523, 2018.
- ⁹Y. Ding, H. Li, H. Sun, L. Wei, B. Jia, H. Su, W. Peng, P. Li, and D. Yu, "A 200-W permanent magnet Hall thruster discharge with graphite channel wall," *Physics Letters A*, vol. 382, pp. 3079–3082, 2018.
- ¹⁰J. Perales-Díaz, A. Domínguez-Vázquez, P. Fajardo, E. Ahedo, F. Faraji, M. Reza, and T. Andreussi, "Hybrid plasma simulations of a magnetically shielded Hall thruster," *Journal of Applied Physics*, vol. 131, no. 10, p. 103302, 2022.
- ¹¹A. Domínguez-Vázquez, "Axisymmetric simulation codes for Hall effect thrusters and plasma plumes," Ph.D. dissertation, Universidad Carlos III de Madrid, Leganés, Spain, 2019.
- ¹²J. Zhou, "Modeling and simulation of the plasma discharge in a radiofrequency thruster," Ph.D. dissertation, Universidad Carlos III de Madrid, Leganés, Spain, 2021.
- ¹³J. Perales-Díaz, A. Domínguez-Vázquez, E. Ahedo, A. Di Sarli, and A. Kitaeva, "Experimentally-informed numerical investigation of a high-power magnetically shielded Hall thruster operating on xenon and krypton," *Journal of Physics D: Applied Physics*, vol. 58, no. 13, p. 135211, 02 2025.
- ¹⁴I. Mikellides, I. Katz, R. Hofer, D. Goebel, K. de Grys, and A. Mathers, "Magnetic shielding of the channel walls in a Hall plasma accelerator," *Physics of Plasmas*, vol. 18, p. 033501, 2011.
- ¹⁵D. Pérez-Grande, O. González-Martínez, P. Fajardo, and E. Ahedo, "Analysis of the numerical diffusion in anisotropic mediums: benchmarks for magnetic field aligned meshes in space propulsion simulations," *Applied Sciences*, vol. 6, no. 11, p. 354, 2016.
- ¹⁶E. Ahedo and V. Pablo, "Combined effects of electron partial thermalization and secondary emission in Hall thruster discharges," *Physics of Plasmas*, vol. 14, p. 083501, 2007.
- ¹⁷S. Araki and R. Wirz, "Magnetic field aligned mesh for ring-cusp discharge chambers," in *50th AIAA/ASME/SAE/ASEE Joint Propulsion Conference & Exhibit*, no. AIAA 2014-3830, Cleveland, Ohio, US, 2014.
- ¹⁸A. Domínguez-Vázquez, J. Zhou, A. Sevillano-González, P. Fajardo, and E. Ahedo, "Analysis of the electron downstream boundary conditions in a 2D hybrid code for Hall thrusters," in *37th International Electric Propulsion Conference*, no. IEPC-2022-338. Boston, MA, USA, June 19-23: Electric Rocket Propulsion Society, 2022.
- ¹⁹J. Perales-Díaz, "Fluid-kinetic models for space plasma thrusters," Ph.D. dissertation, Universidad Carlos III de Madrid, Leganés, Spain, 2024.
- ²⁰I. G. Mikellides, R. R. Hofer, I. Katz, and D. M. Goebel, "Magnetic shielding of Hall thrusters at high discharge voltages," *Journal of Applied Physics*, vol. 116, p. 053302, 2014.
- ²¹N. P. Brown and M. L. R. Walker, "Review of plasma-induced Hall thruster erosion," *Applied Sciences*, vol. 10, no. 11, p. 3775, 2020.
- ²²R. Hofer, S. Cusson, R. Lobbia, and A. Gallimore, "The H9 Magnetically Shielded Hall Thruster," in *35th International Electric Propulsion Conference*, ser. IEPC-2017-232, 2017.
- ²³C. Book and M. Walker, "Effect of anode temperature on Hall thruster performance," *Journal of Propulsion and Power*, vol. 26, no. 5, 2010.
- ²⁴P. Roberts, M. Allen, D. Brick, and B. Jorns, "Empirical closures for momentum and energy transport in Hall thrusters based on Thomson scattering measurements," in *38th International Electric Propulsion Conference, Toulouse, France*, no. IEPC-2024-393, 2024.
- ²⁵J. Perales-Díaz, A. Domínguez-Vázquez, and E. Ahedo, "Simulations of a magnetically-shielded Hall effect thruster with conducting walls," in *38th International Electric Propulsion Conference*, no. IEPC-2024-571. Toulouse, France, June 23-28: Electric Rocket Propulsion Society, 2024.